Wiley Interdisciplinary Reviews: Computational Molecular Science

WILEY

WIREs COMPUTATIONAL MOLECULAR SCIENCE

SOFTWARE FOCUS OPEN ACCESS

A Journey With THeSeuSS: Automated Python Tool for Modeling IR and Raman Vibrational Spectra of Molecules and Solids

Ariadni Boziki[1] | Frédéric Ngono Mebenga[2] | Philippe Fernandes[2] | Alexandre Tkatchenko[1]

[1]Department of Physics and Materials Science, University of Luxembourg, Luxembourg City, Luxembourg | [2]Janssen Research and Development, Pharmaceutical and Material Sciences (PM&S), Janssen Pharmaceutical Companies of Johnson & Johnson, Beerse, Belgium

Correspondence: Alexandre Tkatchenko (alexandre.tkatchenko@uni.lu)

Received: 18 October 2024 | **Revised:** 4 April 2025 | **Accepted:** 8 May 2025

Associate Editor: Peter R. Schreiner | **Editor-in-Chief:** Peter R. Schreiner

Funding: This work was supported by the Janssen Pharmaceutica, THESIS3, European Research Council, MACHINE-DRUG, and Fonds National de la Recherche Luxembourg, BroadApp.

Keywords: DFT | DFTB | IR | machine learning force field | python package | Raman | THz | vibrational spectra

ABSTRACT

Vibrational spectroscopy is an indispensable analytical tool that provides structural fingerprints for molecules, solids, and interfaces thereof. This study introduces THeSeuSS (THz Spectra Simulations Software)—an automated computational platform that efficiently simulates IR and Raman spectra for both periodic and non-periodic systems. Using DFT, DFTB and machine-learning force field, THeSeuSS offers robust capabilities for detailed vibrational spectra simulations. Our extensive evaluations and benchmarks demonstrate that THeSeuSS accurately reproduces both previously calculated and experimental spectra, enabling precise comparisons and interpretations of vibrational characteristics in various test cases, including H_2O and glycine molecules in the gas phase, as well as solid ammonia and solid ibuprofen. Designed with a user-friendly interface and seamless integration with existing computational chemistry tools, THeSeuSS enhances the accessibility and applicability of advanced spectroscopic simulations, supporting research and development in chemical, pharmaceutical, and material sciences.

1 | Introduction

In various industries including chemical, petrochemical, polymer, pharmaceutical, cosmetic, food, and agricultural sectors, there is a pressing demand to enhance product quality and optimize production processes. This has led to a notable resurgence in the application of vibrational spectroscopy [1, 2]. Infrared (IR) and Raman spectroscopy are widely used to probe molecular vibrations, providing complementary information on molecular structure and interactions. Although IR absorption is sensitive to vibrational modes that induce changes in the dipole moment, Raman scattering detects those that alter polarizability [1, 2]. A key region in the vibrational spectra is the fingerprint region (roughly 1500–200 cm^{-1}) which consists of a unique pattern of absorption bands characteristic of specific functional groups. This distinct spectral signature makes the fingerprint region particularly valuable for compound identification, as no two different molecules exhibit the same spectral pattern under identical conditions [3]. Beyond the fingerprint region, the terahertz (THz) region (roughly 200–5 cm^{-1}) has been extensively studied due to its ability to probe low energy vibrational modes, especially in crystalline systems. This spectral range provides critical insight into intermolecular vibrations, which govern molecular orientation and influence key material properties. To

this end, this region offers a "structural fingerprint" by capturing intermolecular vibrations such as lattice/phonon modes. As a result, the analysis of THz and fingerprint regions of the vibrational spectrum serves as a powerful tool for distinguishing different polymorphs and classifying allotropes based on their structural signatures.

Despite significant advancements, deciphering the vibrational spectra of complex compounds remains challenging, particularly for systems with numerous degrees of freedom where intermolecular interactions, such as van der Waals (vdW) forces or extended hydrogen-bonded networks, predominantly govern their properties. The task of assigning peaks in the spectra to specific vibrational modes typically requires a combination of experience and chemical intuition. However, the complexity inherent in these spectra often renders such assignments impractical or even unattainable [4]. Computational methods have been widely used to simulate vibrational spectra across various molecular systems [5–12]. However, the computational cost associated with methods such as coupled-cluster makes them impractical for computing vibrational frequencies of realistically sized molecules, rendering such calculations intensive and often infeasible. Consequently, Density Functional Theory (DFT) has emerged as a widely adopted approach due to its comparatively lower computational demands, making it the method of choice for many theoretical vibrational spectroscopy studies [13–18]. Yet, when investigating large systems such as biomolecules or polymers, even DFT becomes computationally prohibitive. In such cases, alternative approaches such as the density-functional tight-binding (DFTB) method, machine learning models, and classical force fields provide viable solutions to calculate vibrational spectra in complex systems [6, 19–30].

Many electronic structure and classical molecular dynamics codes offer the capability to calculate vibrational frequencies, with some also capable of computing IR intensities and Raman activities. However, these capabilities are less prevalent in codes designed for periodic systems. In such cases, many packages rely on external tools like PHONOPY for phonon frequency calculations, rather than incorporating built-in functions or libraries [31, 32]. Examples of codes adept at simulating vibrational/phonon frequencies and/or IR intensities and Raman activities include FHI-aims [33–37], Quantum ESPRESSO [38, 39], Gaussian [40], GAMESS [41], ORCA [42], TURBOMOLE [43], CP2K [44], SIESTA [45–47], ABINIT [48, 49], CASTEP [50], DFTB+ [51], LAMMPS [52], TRAVIS [53, 54], QERaman [55], MTASpec [56], AiiDA Vibroscopy [57] and others.

Among these, Quantum ESPRESSO, CASTEP, and ABINIT provide highly accurate vibrational spectra by computing IR and Raman responses via Density Functional Perturbation Theory (DFPT). This approach allows for the precise calculation of phonons at any wave vector, ensuring reliable spectral predictions. However, these calculations are computationally demanding and memory-intensive, making them impractical for very large systems. To address this limitation, alternative methods, such as force field-based approaches (LAMMPS), are often employed for large-scale simulations, though they typically sacrifice accuracy for efficiency. Beyond standalone computational packages, automation platforms (AiiDA Vibroscopy, QERaman, MTASpec) have been developed to streamline vibrational spectra calculations by interfacing with electronic structure codes. However, most existing software tools specialize in either quantum-mechanical or semi-classical/fully classical spectrum calculations, and fully integrated frameworks capable of computing both IR and Raman spectra across multiple levels of theory remain relatively rare.

Here, we introduce the THeSeuSS (THz Spectra Simulations Software), a sophisticated Python tool designed for simulating IR and Raman spectra utilizing a static method (diagonalization of the dynamical matrix) at different levels of theory including DFT, DFTB, and a machine-learning force field. Our package provides a fully automated platform that streamlines the spectra calculation process. Users simply provide the experimental crystal structure and input parameters to THeSeuSS, enabling computation of spectra for both periodic and non-periodic systems. This intuitive approach makes it accessible even to novices in the field of vibrational spectroscopy. THeSeuSS interfaces with FHI-aims and DFTB+ for electronic structure calculations and integrates SO3LR [58, 59], for machine learning-based spectra calculations. In contrast to the built-in functionalities of FHI-aims for IR and Raman spectra calculations, our implementation significantly reduces computational time. To optimize calculations of periodic systems, our code interfaces with PHONOPY, leveraging its incorporation of symmetry operations. By selectively displacing coordinates during the finite displacement method, we minimize computational overhead, requiring only calculations for force, polarizability, and Cartesian polarization of irreducible representations. Furthermore, unlike DFTB+, our code extends its capabilities to compute IR intensity and Raman activity for periodic systems. To facilitate the simulation of vibrational spectra in large-scale systems, we have interfaced THeSeuSS with the SO3LR machine learning force field. SO3LR combines the SO3krates neural network for semilocal interactions with universal pairwise force fields to account for short-range repulsion, long-range electrostatics, and dispersion interactions. Trained on a dataset of 4 million neutral and charged molecular complexes at the PBE0, including the many body dispersion (MBD) method level of theory, this model ensures broad coverage of both covalent and non-covalent interactions. Lastly, to further enhance computational efficiency, all single-point calculations associated with the finite displacement method are fully parallelized, thereby further improving computational efficiency.

2 | Methodology

2.1 | IR and Raman Spectroscopy

IR and Raman spectroscopy both involve the interaction between radiation and molecular vibrations. However, they vary in their mechanisms for transferring photon energy to the molecule, which alters its vibrational state. IR spectroscopy relies on transitions between molecular vibrational levels induced by the absorption of mid- and far-IR radiation, a process governed by resonance conditions that involve the electric dipole-mediated transition between energy levels. For a vibrational mode to be deemed "IR active", it must induce changes in the dipole moment without necessarily possessing a permanent dipole [60, 61].

Raman spectroscopy involves a two-photon inelastic light scattering event, where the incident photon carries significantly more energy than the vibrational quantum energy. Part of this energy is transferred to the molecular vibration, causing the remaining energy to be scattered as a photon with reduced frequency. This interaction, characterized by the Raman polarizability of the molecule, occurs under off-resonance conditions. Within a Raman spectrum, the peaks represent the intensity and wavelength of Raman-scattered light, each corresponding to distinct molecular bond vibrations spanning individual and group bonds to lattice modes. In particular, the intensity of Raman spectrum peaks is directly related to both concentration and changes in polarizability [62, 63].

2.2 | Calculation of Vibrational/Phonon Frequencies

Theoretical simulations employ two primary methods to determine vibrational spectra frequencies: the static and dynamic approaches [8]. The static approach, where nuclear positions remain fixed, is commonly employed in various spectroscopic techniques. However, for simulating vibrational spectra of non-rigid and large molecules, exploring the surrounding region of the equilibrium structure and averaging properties of interest from multiple calculations can prove advantageous. Conversely, under certain mechanisms and conditions, such as finite temperature, the dynamic approach is considered superior. In the dynamic approach, nuclear positions evolve according to classical or quantum dynamics, necessitating either first-principles or classical molecular dynamics simulations. Although first-principles molecular dynamics simulations are computationally expensive, especially for large systems, classical molecular dynamics offers an alternative. However, empirical force fields typically apply to specific compounds, such as proteins or polymers, rather than universal models applicable to all systems under study. Given our aim to accommodate systems of varying chemical environments, sizes, and periodicity, we opt for the static approach to calculate vibrational/phonon frequencies.

In the static approach, the nuclear positions are initially optimized at 0 K, followed by displacements of coordinates using either the finite displacement method or DFPT [64–70]. From a computational cost perspective, DFPT has an advantage, particularly for periodic systems, as it enables the exact calculation of phonons at any wave vector. However, the finite displacement method offers a practical advantage. Many popular first-principles codes include implementations for atomic force calculations using various exchange-correlation functionals, pseudo-potential methods, and beyond-DFT approaches, making it readily accessible. In contrast, DFPT implementations may not be as widely available. To ensure user flexibility and accommodate various calculation preferences, the THeSeuSS package employs the finite difference method for calculating vibrational/phonon frequencies.

In perfectly ordered periodic crystals, both IR and Raman spectroscopy reveal distinct peaks corresponding to vibrational modes located at the zone center, a phenomenon attributed to crystal momentum conservation [71]. Phonon calculations carried out at the Γ-point serve as a suitable approach for deciphering the IR and Raman spectra, based on the premise of momentum conservation. This method considers the negligible momentum of visible and IR light in comparison to the size of the Brillouin zone [72].

2.2.1 | Finite Difference Method

The potential energy of a molecule or crystal, denoted as $\mathcal{V}(\mathbf{R})$, where $\mathbf{R}$ represents the atomic positions, can be expanded to a Taylor series. In the harmonic approximation, we approximate the total energy around the equilibrium positions by neglecting terms higher than second order:

$$\mathcal{V}_{Harmonic} = \mathcal{V}\left(\left\{\mathbf{R}_0^{\xi}\right\}_{\xi\in\text{atoms}}\right) + \frac{1}{2}\sum_{\alpha,\beta}\sum_{i,j}\left.\frac{\partial^2\mathcal{V}\left(r_0,\cdots,r_{3|\text{atoms}|}\right)}{\partial R_i^{\alpha}\partial R_j^{\beta}}\right|_{\left\{\mathbf{R}_0^{\xi}\right\}_{\xi\in\text{atoms}}}\Delta R_i^{\alpha}\Delta R_j^{\beta} \tag{1}$$

where the atoms are indexed with α,β and $i,j = x,y,z$ are cartesian indices. The linear term is eliminated, as the system experiences no forces while in equilibrium.

While first derivatives are relatively straightforward to compute, the same cannot be said for second derivatives. Equation (1) involves the second derivative of energy with respect to atomic displacements from equilibrium, known as the matrix of force constants or the Hessian. The Hessian elements, $\mathcal{H}_{i,j}^{\alpha,\beta} = \frac{\partial^2\mathcal{V}}{\partial R_i^{\alpha}\partial R_j^{\beta}}$, can be assessed by numerically computing the second-order derivative using finite differences.

$$\begin{aligned}\mathcal{H}_{i,j}^{\alpha,\beta} &= \left.\frac{\partial^2\mathcal{V}}{\partial R_i^{\alpha}\partial R_j^{\beta}}\right|_{\left\{\mathbf{R}_0^{\xi}\right\}_{\xi\in\text{atoms}}} = -\left.\frac{\partial}{\partial R_i^{\alpha}}F_j^{\beta}\right|_{\left\{\mathbf{R}_0^{\xi}\right\}_{\xi\in\text{atoms}}} \\ &= -\lim_{\varepsilon\to 0}\sum_{\hat{\imath}}\frac{F_j^{\beta}\left(\mathbf{R}_0^{\alpha}+\varepsilon\hat{\imath}\right)}{\varepsilon},\end{aligned} \tag{2}$$

where F_j^{β} represents the force applied to the coordinate j of atom β when coordinate i of atom α is displaced and $\hat{\imath}$ stands for the unit axial directional vectors.

To compute the second derivative, this process is repeated for all 3N Cartesian coordinates. Each atomic coordinate undergoes incremental adjustments: first, it is increased by a small amount $(+\frac{1}{2}\delta)$, where δ is the displacement, and the gradients are calculated. Then, the coordinate is decreased $(-\frac{1}{2}\delta)$, and the gradients are recalculated. The second derivative is then determined using the two-point central difference formula.

$$\begin{aligned}\mathcal{H}_{i,j}^{\alpha,\beta} &= \sum_{\hat{\imath}}\frac{\mathbf{F}^{\alpha}\left(\mathbf{R}_0^1,\cdots,\mathbf{R}_0^{\beta}+\hat{\imath}\frac{\delta}{2},\cdots\right)-\mathbf{F}^{\alpha}\left(\mathbf{R}_0^1,\cdots,\mathbf{R}_0^{\beta}-\hat{\imath}\frac{\delta}{2},\cdots\right)}{\delta} \\ &\coloneqq \frac{1}{\delta}\sum_{\hat{\imath}}\Delta_{\beta\hat{\imath}}\mathbf{F}^{\alpha}\end{aligned} \tag{3}$$

Because the Hessian is symmetric, $\mathcal{H}_{i,j} = \mathcal{H}_{j,i}$, random errors arising from gradient calculations can be mitigated (by a factor of $(1/2)^{(1/2)}$) by redefining the Hessian as follows:

$$\mathcal{H}_{i,j}^{\alpha,\beta} = \frac{1}{2\delta} \sum_{\hat{\imath}} \left(\Delta_{\alpha\hat{\imath}} \mathbf{F}^{\beta} + \Delta_{\beta\hat{\imath}} \mathbf{F}^{\alpha} \right) \tag{4}$$

This matrix represents the force constants for the system. Prior to calculating the vibrational frequencies, it must be mass-weighted:

$$\mathcal{H}_{i,j}^{\alpha,\beta} = \frac{\mathcal{H}_{i,j}^{\alpha,\beta}}{\sqrt{M_i^{\alpha} M_j^{\beta}}}. \tag{5}$$

By diagonalizing the mass-weighted Hessian matrix, the eigenvectors $\{Q_l\}$ of it represent the vibrational normal modes, while the corresponding eigenvalues provide the vibrational frequencies $\{\omega_l\}$.

However, an added complexity arises when dealing with periodic boundary conditions, as we must also consider the atoms within the unit cell along with their periodic images. In the finite-displacement supercell approach, first-principles calculations serve as the foundation for obtaining atomic forces within a supercell crystal structure model. Force constants are derived from multiple supercells, each subjected to different sets of displacements. Phonons are computed exactly (i.e., without interpolation) from the force constants of the supercell at wave vectors commensurate with its shape relative to the primitive cell. For other wave vectors, the phonons are obtained by interpolation. Typically, using a supercell size containing a few hundred atoms yields reasonable phonon results through interpolation, although the required accuracy may vary depending on the specific calculation objectives [31]. In our approach, phonon frequencies are calculated using the PHONOPY package. A detailed mathematical description of how to calculate the phonon frequencies of periodic systems is given by *Togo* [31].

2.3 | IR Intensity

The standard IR spectrometer employs a broad-band source that simultaneously emits all IR frequencies of interest. These frequencies cover the near-IR region (14,000–4000 cm^{-1}), the mid-IR region (4000–400 cm^{-1}), and the far-IR region (400–10 cm^{-1}) [73]. As previously discussed, a well-known selection rule in IR spectroscopy dictates that a change in dipole moment during vibration renders the mode IR active [4, 74]. More specifically, IR absorption occurs via an electric dipole operator-mediated transition, wherein the change in dipole moment relative to a change in vibrational amplitude is greater than zero.

The IR intensity, denoted as I_i, for the ith vibrational normal mode within the double-harmonic approximation, can be expressed as follows:

$$I_i \propto \left(\frac{\partial \boldsymbol{\mu}}{\partial Q_i} \right)^2. \tag{6}$$

Here, we omit proportionality factors and quantum corrections, Q_i represents the ith normal coordinate and $\boldsymbol{\mu}$ denotes the system's dipole moment [8]. The definition of $\boldsymbol{\mu}$ is typically applicable only to isolated molecules, where periodic boundary conditions are absent. However, in periodic systems, the Berry phase approach to polarization and maximally localized Wannier functions (MLWFs) have proven successful in addressing this limitation [75–79].

To determine the IR intensity (as defined in Equation (6)), our methodology involves several steps. Initially, we compute the dipole moment for both FHI-aims and DFTB+ in non-periodic systems. For periodic systems, in the case of FHI-aims, we calculate the Cartesian polarization utilizing the Berry phase approach to polarization and MLWFs, while in the case of DFTB+ we calculate the dipole moment for periodic systems. Following this, we determine the derivative through the application of finite differences [80, 81]. Currently, when utilizing SO3LR, IR intensity calculations are not supported.

2.4 | Raman Activity

Raman spectroscopy operates on the principle of inelastic light scattering, spanning the near-infrared, visible, and near-ultraviolet regions of the electromagnetic spectrum. As mentioned above, for Raman bands to be detected, molecular vibrations must induce a change in polarizability. Thus, a fundamental component crucial for simulating Raman intensity is the electronic static polarizability tensor, represented as $\widetilde{\alpha}$.

In Raman spectroscopy, two types of Raman scattering are observed: Stokes and anti-Stokes. Stokes Raman scattering occurs when molecules initially in the ground vibrational state undergo scattering, while anti-Stokes Raman scattering occurs when molecules initially in a vibrational excited state undergo scattering [73]. In most experimental setups, a plane-polarized laser beam serves as the incident beam, with the incident beam's direction, polarization orientation, and the observation direction all mutually perpendicular. Under these conditions, the first-order differential Raman cross-section, specifically for the Stokes component of the ith eigenmode far from resonance, within the double-harmonic approximation, is as follows: [74].

$$\frac{\partial \sigma_i}{\partial \Omega} = \frac{\left(2\pi \nu_s\right)^4}{c^4} \frac{h\left(n_i^b + 1\right)}{8\pi^2 \nu_i} \frac{I^{\mathrm{Ram}}}{45} \tag{7}$$

where ν_s and ν_i are the wavenumbers of the scattered light and the ith normal coordinate, respectively, n_i^b is the Bose-Einstein statistical factor, expressed as:

$$n_i^b = \left[\exp \frac{h\nu_i}{kT} - 1 \right]^{-1}. \tag{8}$$

and I^{Ram} is the Raman-scattering activity: [74].

$$I^{\mathrm{Ram}} = 45\left(\frac{\partial \alpha}{\partial Q} \right)^2 + 7\left(\frac{\partial \beta}{\partial Q} \right)^2 = 45\alpha'^2 + 7\beta'^2. \tag{9}$$

In Equation (9), α' is the mean polarizability derivative and β'^2 is the anisotropy of the polarizability tensor derivative. The expressions for α' and β'^2 are given by:

$$\alpha' = \frac{1}{3}\left(\widetilde{\alpha}'_{xx} + \widetilde{\alpha}'_{yy} + \widetilde{\alpha}'_{zz}\right), \tag{10}$$

$$\beta'^2 = \frac{1}{2}\left[\left(\widetilde{\alpha}\prime_{xx} - \widetilde{\alpha}\prime_{yy}\right)^2 + \left(\widetilde{\alpha}\prime_{xx} - \widetilde{\alpha}\prime_{zz}\right)^2 + \left(\widetilde{\alpha}\prime_{yy} - \widetilde{\alpha}\prime_{zz}\right)^2\right] + 6\left(\widetilde{\alpha}\prime^2_{xy} + \widetilde{\alpha}\prime^2_{xz} + \widetilde{\alpha}\prime^2_{yz}\right). \tag{11}$$

From a computational standpoint, the Raman activity serves as the basis for our calculations in the Raman spectrum.

To determine the Raman activity (as defined in Equation (9)), we undertake several steps. Initially, we computed the polarizability matrix for both FHI-aims and DFTB+ in both periodic and non-periodic systems. For FHI-aims, we employ DFPT, while for DFTB+, polarizability is evaluated using coupled-perturbed linear response (CPLR) [82]. Subsequently, akin to the procedure for IR intensity determination, we derive the necessary derivative using finite differences [80, 81]. Currently, when using SO3LR, Raman activity calculations are not supported.

3 | Features of the Code

TheSeuSS is a fully automated tool designed to streamline the calculation of IR and Raman spectra for a wide range of systems, from small molecules to large molecules and crystals. It consists of the following components:

1. Conversion of Experimental Geometry Input: Converts .cif format files containing experimental structures into either FHI-aims, DFTB+, or SO3LR geometry input files (only for periodic systems).
2. Space Group Determination of the Experimental Structure: Determines the space group of the experimental crystal structure (only for periodic systems). This determination is facilitated by the Spglib library, a software for crystal symmetry search [83].
3. Geometry Optimization: Optimizes the geometry for both periodic and non-periodic systems as well as the cell for periodic systems. Depending on the chosen method (whether DFT, DFTB or machine-learning force field), users have access to a wide range of functionals, dispersion method models, and simulation parameters provided by FHI-aims for DFT calculations. Similarly, for DFTB calculations, users can utilize various models for dispersion interactions and simulation parameters provided by DFTB+ software. When performing geometry optimization with the SO3LR machine learning model, users can choose from several optimization algorithms to best suit their needs.
4. Space Group Determination of the Optimized Structure: Identifies the space group of the optimized crystal structure (only for periodic systems).
5. Vibrational/Phonon Frequency Calculations: Utilizes the finite difference method to compute vibrational or phonon frequencies. For non-periodic systems, TheSeuSS includes built-in functions, while for periodic systems, the PHONOPY code is employed [31, 32]. This part, along with the following section, is the most time-consuming. To address this, we have parallelized these components. In essence, following the finite difference method described in the Methodology section, each atomic coordinate undergoes incremental adjustments, both increased and decreased by the same small amount. Subsequently, a single-point calculation is performed for each case to calculate the gradient using Equation (4). This process is repeated for all coordinates of all atoms in the system under study, particularly for the non-periodic case. To accelerate the frequencies computation, we utilize the ThreadPoolExecutor from Python's concurrent.futures module, enabling parallel execution of the single-point calculations. In the case of periodic systems, leveraging PHONOPY introduces an additional efficiency feature. PHONOPY inherently accounts for the symmetry of the crystal structure, thereby reducing the necessary single-point calculations to only those atomic coordinates that comprise the irreducible representation. This significantly reduces the number of calculations required for periodic systems.
6. Property Calculations: For both periodic and non-periodic systems, while the FHI-aims code is used, DFPT calculations are performed to determine the polarizability matrix. When employing the DFTB+ code, we instead conduct CPLR calculations for the same purpose. Additionally, for periodic systems analyzed with FHI-aims, cartesian polarization is calculated using the Berry phase method and MLWFs. In both coding environments, the dipole moment is determined for non-periodic systems. Moreover, when using DFTB+, the dipole moment for periodic systems is also assessed. We employ the same parallelization scheme described earlier (part 5). For periodic systems, the calculations of these properties are performed for coordinates comprising the irreducible representation, as defined by the symmetry operations applied by PHONOPY. Utilizing the Spglib library [83], we match atoms to their counterparts within the irreducible representation, enabling the construction of the full matrix for subsequent calculations of IR intensity and Raman activity. Currently, when using SO3LR, the calculation of dipole moment/cartesian polarization and the polarizability matrix is not supported.
7. IR Intensity and Raman Activity: Computes the IR intensity from the dipole moment or the cartesian polarization and the Raman activity from the polarizability matrix. Currently, when using SO3LR, the computation of IR intensity and Raman activity is not supported.
8. Spectra Calculation: Utilizes the acquired vibrational/phonon frequencies, IR intensity, and Raman activity to generate the system's IR and Raman spectra. In addition to the raw spectral data, TheSeuSS offers internal built-in functions for spectrum plotting, allowing users to apply either Gaussian or Lorentzian broadening based on their preference.

The code can execute all its components simultaneously or individually, depending on the user's preference. This choice is customizable within the input file. Comprehensive details

on the input file and usage examples can be found in the THeSeuSS documentation [84]. Beyond its utility as a tool to simulate IR and Raman spectra, THeSeuSS serves as an automation tool for structure optimization. Users can input experimental structures, and with its built-in functions, THeSeuSS can convert .cif format files into suitable inputs for FHI-aims, DFTB+ or SO3LR. Additionally, it can serve solely as a spectrum generation tool if users have already computed frequencies, IR intensities, and Raman activities using alternative methods. Furthermore, THeSeuSS is capable of calculating THz spectra, where only the frequencies of the spectrum are computed. In Figure 1, we provide a concise overview of the algorithmic protocol used to generate the IR and Raman spectra.

4 | Evaluating and Benchmarking THeSeuSS

To evaluate the capability of the code in generating vibrational spectra, we selected both non-periodic and periodic systems for testing and benchmarking. For the non-periodic systems, we selected an H_2O molecule and a glycine molecule, both in the gas phase. For periodic systems, we chose the ammonia molecular crystal from the X23 database [85, 86], and ibuprofen [2-(4-isobutylphenyl) propionic acid] molecular crystal, known for its non-steroidal anti-inflammatory, analgesic, and antipyretic properties.

For the tests and benchmarks associated with the FHI-aims code in periodic systems, we have chosen the PBE functional

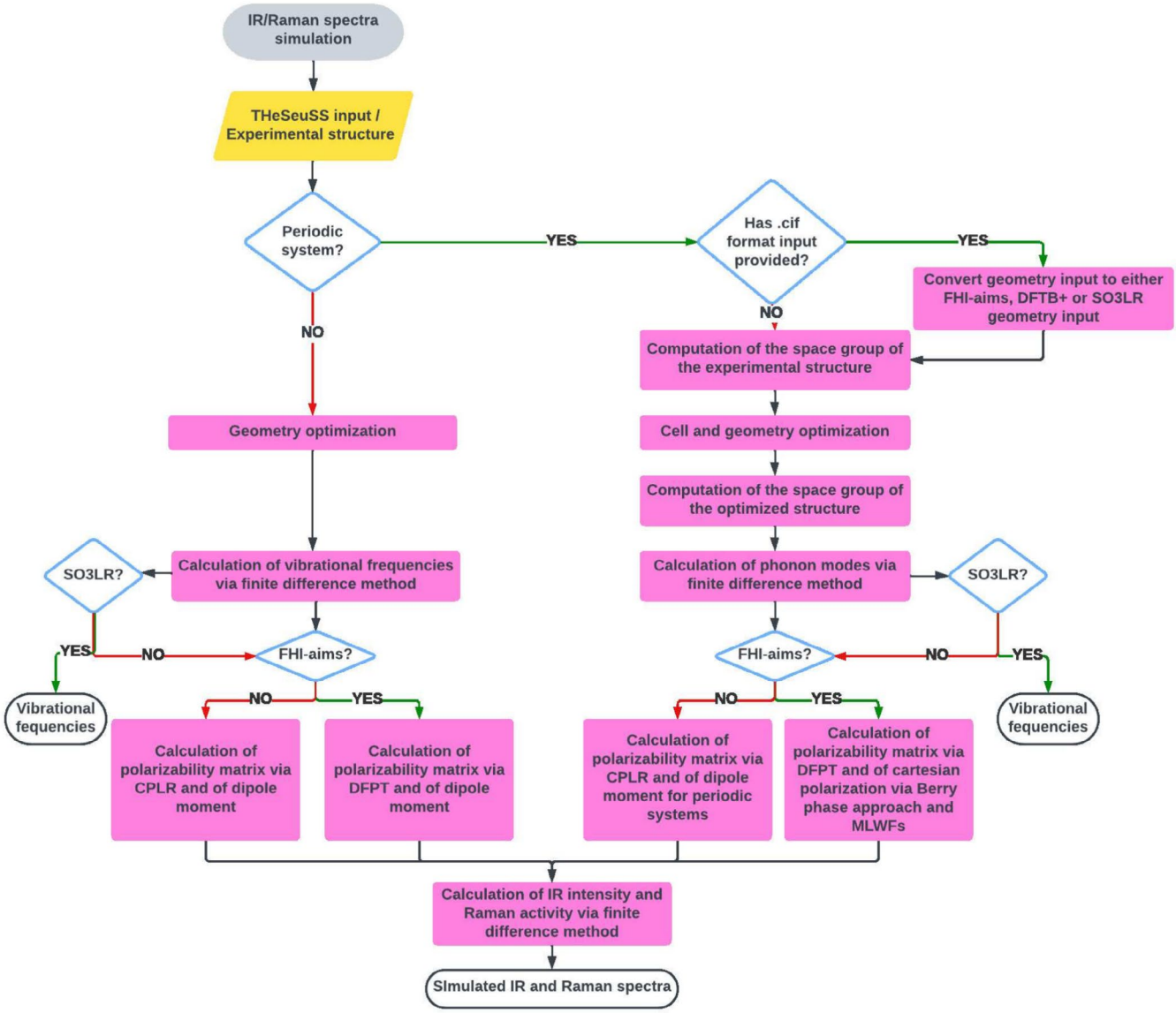

FIGURE 1 | Algorithmic Protocol for Calculating IR and Raman Spectra: This entire process has been automated within our developed package THeSeuSS. The procedure begins with the optimization of the experimental crystal structure. Following this, we employ the finite difference method to compute vibrational/phonon frequencies. For FHI-aims, DFPT is employed to calculate the polarizability matrix for each displaced structure, while for DFTB+, we use the CPLR. Additionally, in the case of periodic systems using FHI-aims, the Berry phase method and MLWFs are applied to calculate the cartesian polarization. Once modes are classified as IR or Raman active, we calculate the IR intensity using the dipole moment/cartesian polarization and the Raman activity using the polarizability matrix. These calculated frequencies, alongside the IR intensity and Raman activity, are then utilized to generate the simulated spectra.

[87], supplemented by the nonlocal many-body dispersion (MBD-NL) method [88]. This selection is backed by extensive benchmarks established by the Crystallographic Data Centre (CCDC) through blind tests that assess computational methods capable of precisely describing the intricate nature of molecular crystals [89–92]. Although these benchmarks highlight the hybrid PBE0 functional [93], along with the MBD approach [94–97], we opted for the PBE functional due to its lower computational demands for DFPT calculations of the polarizability matrix, which are generally four times more resource-intensive than a single force evaluation [28, 80]. For non-periodic systems, we utilize several functionals (PBE, PBE0, B3LYP) [98, 99] both with and without the MBD-NL method, with some results reported in the Supporting Information. For the DFTB+ code, we employed the MBD method and performed vibrational spectra simulations at the third-order Density Functional Tight Binding (DFTB3 + MBD) level.

In Figure 2, we present the simulated IR and Raman spectra of a H_2O molecule in the gas phase. To assess the accuracy of our approach in capturing vibrational spectra, we compare our results with data from previous calculations [100]. This choice is driven by the nature of available experimental data, which predominantly feature H_2O clusters in liquid, gas, or solid states, rather than isolated molecules. In these states, hydrogen-bonding networks break the symmetry of the molecular structure, leading to qualitatively different vibrations compared to those of isolated molecules. This phenomenon is also evident in several studies that report computed vibrational frequencies of small water clusters at the CCSD(T) level [100–105]. These studies focus primarily on calculating vibrational frequencies and other properties for small water clusters, $(H_2O)_n$, where $n = 2 - 6$. They demonstrate that as the cluster size increases from dimer to trimer and beyond, the vibrational frequencies differ for each distinct water cluster. As detailed in Table S1, in the gas phase, the H_2O molecule displays two types of stretching vibrations (symmetric and antisymmetric) and a bending vibration [100, 106–108]. To quantitatively compare our simulated spectra with reference data, we use the mean absolute percentage error (MAPE), calculated as follows:

$$\text{MAPE} = \frac{100}{N} \times \sum_{i=1}^{N} \left| \frac{y_i - \hat{y}_i}{y_i} \right|. \tag{12}$$

Additionally, we assess the frequency shifts as percentages, defined by:

$$\text{Shift Percentage} = 100 \times \left| \frac{y_i - \hat{y}_i}{y_i} \right|. \tag{13}$$

In these equations, y_i represents the reference data, and $\hat{y}_i$ denotes our simulated results.

Table S1 of the Supporting Information shows that the simulated spectra at the PBE0 + MBD-NL level show excellent agreement with the reference data, particularly in accurately describing vibrational frequencies. As expected, the results of hybrid functionals (PBE0, B3LYP) outperform those obtained with the PBE functional. The use of MBD-NL did not affect the results as this method primarily addresses long-range dispersion forces. However, it is important to note that hybrid functionals (PBE0 and B3LYP) are not implemented in the DFPT framework of FHI-aims. Consequently, when TheSeuSS performance is evaluated with a hybrid functional, the polarizability matrix and in turn Raman activity are computed at the corresponding PBE or PBE + MBD-NL levels. SO3LR demonstrates excellent agreement with the reference data, offering a computationally efficient and cost-effective method for calculating the vibrational frequencies of molecular systems.

In contrast, the DFTB3 + MBD method demonstrates more substantial deviations from the reference data, a result that aligns with expectations given the limitations of the DFTB approach arising from the semi-empirical nature of the method [109–111]. The deviations observed in our simulations using THeSeuSS should not be interpreted as deficiencies in our implementation. In fact, several studies have been conducted to improve the accuracy of the DFTB parameterization for water

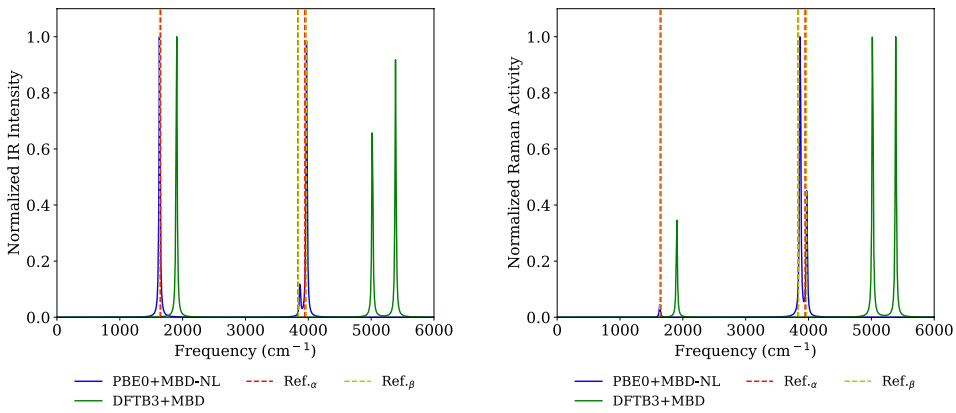

(a) IR spectra of H_2O molecule in gas phase.

(b) Raman spectra of H_2O molecule in gas phase.

FIGURE 2 | Simulated IR and Raman spectra of a H_2O molecule in the gas phase, calculated at both the PBE0 + MBD-NL and DFTB3 + MBD levels, compared with reference data [100]. Abbreviations: Ref. $_\alpha$: Reference data obtained with CCSD(T) and ha5Z basis set, Ref. $_\beta$: Reference data obtained with MP2 and ha5Z basis set.

[112–115] However, exploring these alternatives is beyond the scope of this paper; therefore, we have focused solely on the DFTB3 + MBD method without benchmarking different DFTB parameterizations. Despite these challenges, we will present all data related to DFTB to ensure a comprehensive analysis of our implementation.

Furthermore, we address the challenges of analyzing the vibrational spectra of the glycine molecule in the gas phase, primarily hindered by its low thermal stability. Achieving a sufficient gas-phase concentration of glycine to record its vibrational spectra is not feasible, which significantly impedes these studies. Researchers have often resorted to alternative methods, such as combining IR spectroscopy with matrix isolation techniques [116–119].

Quantum mechanical calculations reveal three stable conformers of glycine, referred to as conformers I, II, and III [116]. If all three conformers are present in a sample, the resulting experimental vibrational spectrum would likely be a superposition of their individual spectra, adding a layer of complexity to accurate measurements. For our benchmarks, we focused on conformer I. The molecular point group of this conformer, C_s, allows all 24 of its vibrational modes to be active in both IR and Raman spectroscopy.

Using THeSeuSS at various theoretical levels, including PBE + MBD-NL, DFTB3 + MBD, PBE, PBE0, PBE0 + MBD-NL, B3LYP, and SO3LR (as detailed in the Supporting Information), we successfully identified all 24 vibrational modes, ranging from strong and medium to weak intensity bands. However, it is notable that experimental IR and Raman spectra typically display only the strongest or medium intensity bands, often reporting fewer than 24 bands in the literature. Our simulated spectra, shown in Figure 3, along with previously established calculations and experimental frequencies, are presented [116, 117].

To ensure a quantitative comparison of our implementation, we calculated the MAPE and frequency shifts, both expressed as percentages (see Table S2), relative to prior calculations rather than experimental data, which could lack complete spectral bands and potentially be misleading due to the presence of multiple conformers. This approach guarantees a precise, one-to-one comparison, crucial for an accurate assessment of our implementation.

As demonstrated in Table S2 of the Supporting Information, the simulated spectra at the PBE + MBD-NL level show good agreement with the reference data, particularly in accurately describing the vibrational frequencies. Some bands exhibit frequency shifts, probably because of the absence of anharmonic effects in our implementation. Similar frequency shifts are observed with SO3LR machine-learning force field model and hybrid functionals such as PBE0 and B3LYP, and MBD-NL does not affect the results, similar to the H_2O molecule in the gas phase case. In contrast, the DFTB3 + MBD method reveals more significant deviations from the reference data, consistent with the expected

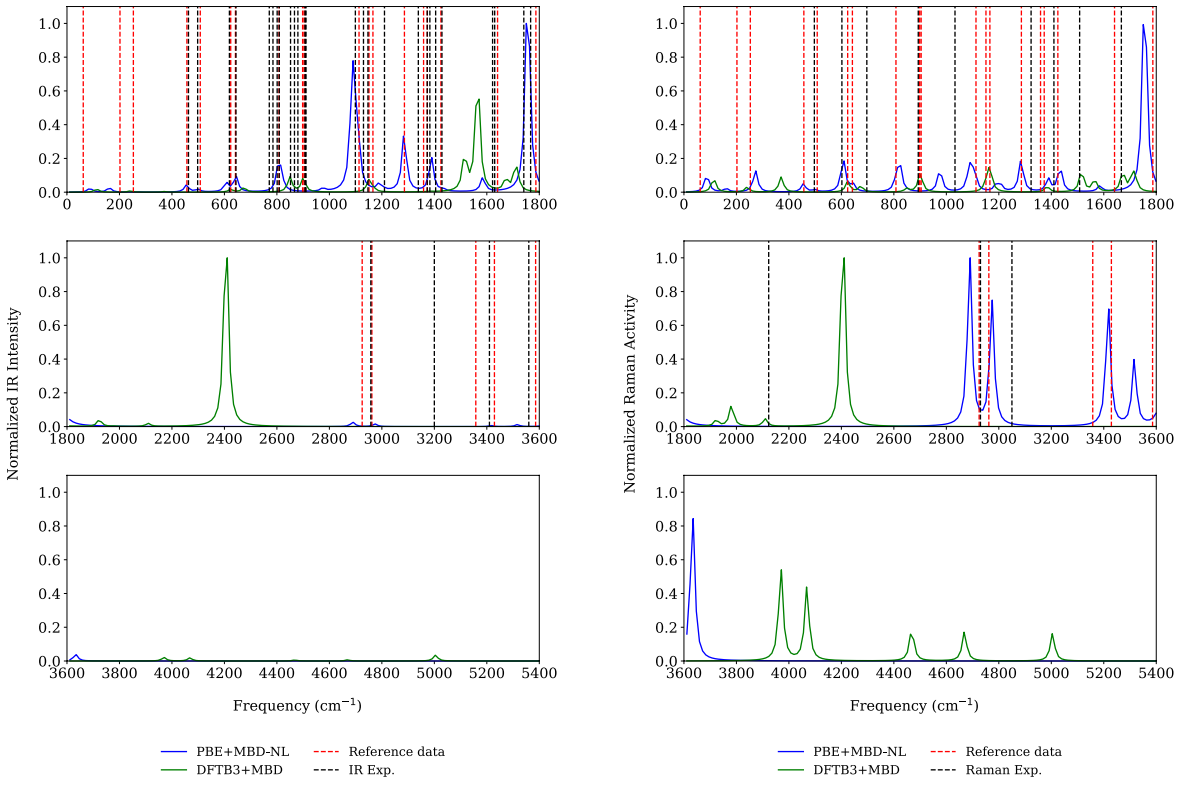

(a) IR spectra of glycine molecule in gas phase.

(b) Raman spectra of glycine molecule in gas phase.

FIGURE 3 | Vibrational spectra of a glycine molecule in the gas phase: (a) IR spectra calculated using both PBE + MBD-NL and DFTB3 + MBD levels, compared with previously established calculations and experimental IR frequencies [116]. (b) Raman spectra calculated at both the PBE + MBD-NL and DFTB3 + MBD levels, compared with previously established calculations and experimental Raman frequencies [116, 117]. Abbreviations: IR Exp.: Experimental IR frequencies, Raman Exp.: Experimental Raman frequencies.

limitations of the DFTB approach. Despite these deviations, we present DFTB data for glycine to provide a comprehensive analysis of our implementation.

It is noteworthy that the deviations between our simulated frequencies and the experimental data (Figure 3) are consistent with those between the experimental data and the reference data used in our study of glycine, despite both sets of data originating from the same study [116]. This alignment suggests that the discrepancies between our simulated frequencies and the experimental frequencies do not indicate deficiencies in our implementation. Instead, in the case of the glycine molecule in the gas phase, they reflect the inherent limitations of experimental techniques, which often fail to capture complete spectral bands and can be influenced by the presence of multiple conformers (Figure 4).

In addition to comparing our simulated results with reference data, a crucial aspect of our analysis is assigning specific frequencies to particular vibrations. For instance, the C═O stretching vibrations are identified at a calculated mode of approximately 1756 cm^{-1}. The mode at 1585 cm^{-1} corresponds to O–H bending vibrations. The frequency range between 808 and 1400 cm^{-1} encompasses C–O and C–C stretching vibrations, with a subset from 822 to 1189 cm^{-1} also encompassing CNH bending vibrations. Additionally, N–H stretching vibrations appear between 3417 and 3516 cm^{-1}, and O–H stretching is observed at 3633 cm^{-1}. Low frequency ranges from 87 to 643 cm^{-1} are associated with various torsional and bending vibrations, including NCC-O and NCC═O torsion, NCC bending, CCNH torsion, and CCOH torsion and bending. These assignments, based on our PBE + MBD-NL data, align with previously reported mode assignments [116, 117].

To evaluate and benchmark the performance of THeSeuSS on periodic systems, we chose phase I of solid ammonia, which crystallizes in the cubic $P2_13$ structure, as a test case. Despite numerous reports over the past 50 years detailing the IR and Raman spectra of solid ammonia's different phases, these studies often present conflicting spectral characteristics [120–127]. Notably, to the best of our knowledge, there have been no previously computed IR and Raman spectra for phase I of solid ammonia.

In assessing the accuracy of our implementation to describe vibrational spectra, we compare our simulated spectra with the most recent experimental data, as illustrated in Figure 4 and detailed in Table S3 of Supporting Information [120, 121]. It is important to note that these experimental results focus primarily on the most intense bands, omitting a comprehensive list of all vibrational modes. Consequently, we opt for a distinct approach to quantitative analysis, which differs from our methodology for analyzing the vibrational frequencies of H_2O and glycine molecules in the gas phase. Our simulations capture frequencies corresponding to both strong and weak bands. However, in Table S3, we specifically list the simulated frequencies of the most intense bands, with a few exceptions for weak bands in the Raman spectrum, enabling one-to-one comparison with the experimental data.

More specifically, in the case of IR spectra analyzed using PBE + MBD-NL, the primary modes show close alignment between the computed spectra from TheSeuSS and the experimental spectra. Notably, there is an additional main mode present in the computed spectra that is absent in the experimental data. However, the frequency shifts and MAPE for the four modes that can be compared across both datasets show good agreement. Furthermore, as indicated in Table S3, the assignments of these modes correspond well to the computed and experimental spectra.

In contrast, when using DFTB3 + MBD, the mode assignments do not align as closely, and the frequency shift for the 946 cm^{-1} mode is significant. In addition, two more main modes are observed at lower frequencies. It is crucial to note that a low MAPE value, calculated using only the three modes that correspond between the experimental and simulated spectra, does not necessarily reflect an accurate spectrum description. These deviations are consistent with the known limitations of the DFTB approach, as previously discussed. However, DFTB3 + MBD

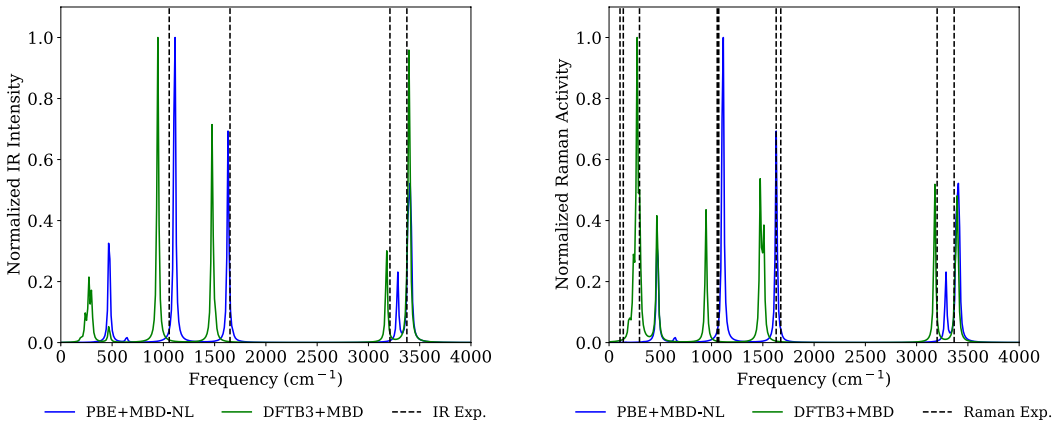

(a) IR spectra of ammonia in solid phase (phase I). (b) Raman spectra of ammonia in solid phase (phase I).

FIGURE 4 | Vibrational spectra of ammonia in solid phase (Phase I): (a) IR spectra calculated at both the PBE + MBD-NL and DFTB3 + MBD levels, alongside experimental IR frequencies [120]. (b) Raman spectra similarly calculated and compared with experimental Raman frequencies [121]. Abbreviations: IR Exp.: Experimental IR frequencies, Raman Exp.: Experimental Raman frequencies.

demonstrates improved performance in analyzing the IR spectrum of solid ammonia compared to its performance with H_2O and glycine molecules in the gas phase.

Similarly, in the case of Raman spectra, PBE + MBD-NL demonstrates superior performance, particularly evident in its treatment of high-frequency modes, where it demonstrates good agreement with the experimental data in terms of frequency shifts. Although our simulated spectra exhibit weak bands in the low-frequency modes, we include them in our analysis for a more comprehensive understanding. Notably, the mode at 160 cm^{-1}, although not prevalent in recent experimental spectra, has been reported by Binbrek et al. [125]. We speculate that its absence in recent publications could be attributed to its association with a weak band. It is conceivable that employing the PBE0 + MBD-NL method could further enhance the agreement of these low-frequency modes.

To further examine THeSeuSS's efficiency with more complex systems, we calculated the IR and Raman spectra of solid ibuprofen, a widely used drug for managing and treating inflammatory diseases. The Raman spectra can be found in Supporting Information. Solid ibuprofen crystallizes in the $P2_1/c$ space group. In Figure 5 we present the simulated IR spectra of solid ibuprofen alongside the experimental IR frequencies. The displayed vibrational frequencies correspond to medium, strong, and very strong bands, while frequencies associated with weak and very weak bands are omitted. This Figure demonstrates that THeSeuSS effectively reproduces the IR spectrum of solid ibuprofen, a conclusion further supported by the frequency shifts expressed as percentages shown in Table S4. This indicates that PBE + MBD-NL accurately calculates the IR frequencies of the system. In particular, the simulated vibrational frequencies calculated at the DFTB3 + MBD level also show better agreement with the experimental data (at least for the modes with experimental counterparts) compared to the previous systems we examined. This is also evident in Figure S1 and Table S5, which present the calculated Raman spectra of ibuprofen along with the experimental data. The reasons behind this outcome warrant further investigation, as we hypothesize that the crystal structure of ibuprofen and its molecular interactions may play a significant role. Although this study provides a comprehensive analysis of the high-frequency region, the THz region (shown in the inset of Figure 5) has not yet been thoroughly examined. Given that ibuprofen consists of larger molecules, we assume that long-range interactions play a more significant role in its vibrational properties. Since DFTB3 is coupled with MBD, (an accurate method for describing intermolecular interactions), DFTB3 + MBD could be expected to show good agreement with the experimental data for this system. However, discrepancies between the two methods (PBE + MBD-NL and DFTB3 + MBD) persist in the THz region, particularly in the calculated intensities. Future work will aim to further investigate this aspect and provide a more comprehensive understanding of the underlying factors that contribute to these differences.

It is crucial to note that we have not yet discussed spectral intensities or compared our simulated results with experimental intensities. Discrepancies between the simulated and experimental intensities are expected primarily because of variations in the settings of the experimental apparatuses. Specifically, in Raman spectroscopy, the accurate calculation

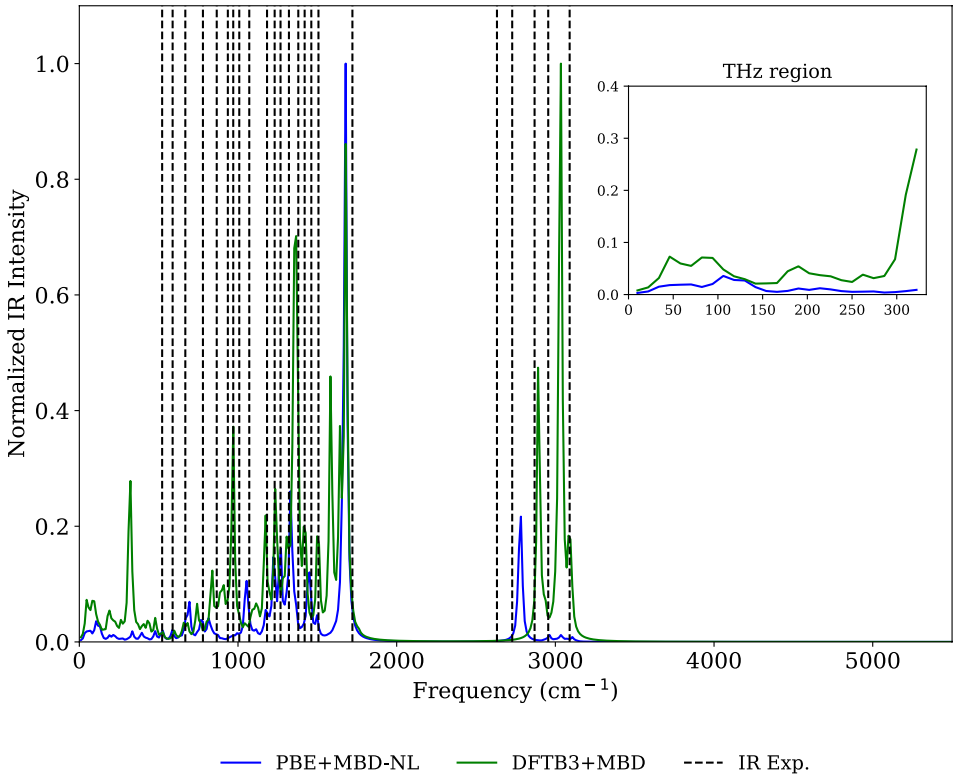

FIGURE 5 | IR spectrum of ibuprofen in solid phase calculated at both the PBE + MBD-NL and DFTB3 + MBD levels, alongside experimental IR frequencies [128]. Abbreviations: IR Exp.: Experimental IR frequencies.

of Raman activity using Equation (9) requires that the incident beam's direction, polarization orientation, and observation direction be mutually perpendicular. However, this ideal alignment is not always achievable in experimental setups, leading to potential disparities between experimental and calculated intensities. In future work, we will further investigate these intensity variations and explore differences across various levels of theory.

Consequently, IR intensity and Raman activity should be regarded as theoretical estimates. Discrepancies from the experimental intensities are anticipated and should not be seen as limitations of our implementation. It is worth mentioning that this approach is common across most computational codes that calculate IR and Raman intensities, reflecting a standard practice in theoretical spectroscopy.

5 | Conclusions

We have developed THeSeuSS, an automated computational platform designed to improve the efficiency of simulating IR and Raman spectra. This Python-based package adeptly captures the complex details of vibrational spectra, requiring only the system's crystal structure and minimal additional input from the user. This streamlined approach makes it accessible even to those with limited experience in spectroscopy, enabling them to compute spectra with ease. THeSeuSS is capable of generating spectra using the DFT, DFTB, and machine-learning force field methods. It employs a static approach to calculate vibrational frequencies and leverages the calculated dipole moments, cartesian polarization, and polarizability matrices to determine IR intensity and Raman activity, delivering high-fidelity spectral data for both periodic and non-periodic systems.

TheSeuSS interfaces with FHI-aims for DFT-level calculations, with DFTB+ for DFTB-level calculations, and SO3LR for calculations at machine-learning force field level ensuring broad compatibility. For phonon frequency analysis in periodic systems, it interfaces with PHONOPY, whereas for non-periodic systems, it utilizes specially developed built-in functions. TheSeuSS offers a comprehensive suite of functionalities: (1) conversion of experimental geometry inputs, (2) determination of space group for both experimental and optimized structures, (3) geometry optimization, (4) vibrational or phonon frequency calculations, (5) calculation of properties such as dipole moments and polarizability matrices, (6) calculation of IR intensity and Raman activity, and (7) generation of spectra. Users can operate these components either simultaneously or individually, tailoring the process to their specific needs. Additionally, TheSeuSS can also compute THz spectra, focusing solely on the calculation of spectral frequencies.

To minimize computational time, we have implemented parallelization across several key components of the code. Specifically, the single-point calculations required for the finite difference method, used in determining vibrational/phonon frequencies and other properties, are fully parallelized. Additionally, by integrating PHONOPY and leveraging its ability to recognize the symmetry of the crystal structure, we have introduced an efficiency enhancement. This integration reduces the number of necessary single-point calculations by limiting them to only those atomic coordinates within the irreducible representation.

Our evaluations across diverse molecular and solid systems; including non-periodic systems like H_2O and glycine molecules, as well as the periodic systems phase I of solid ammonia, and solid ibuprofen highlight THeSeuSS's ability to reliably reproduce IR and Raman spectra. These results closely align with both experimental data and previously established calculations.

Our developed code, THeSeuSS, has implications across multiple industries that depend on vibrational spectroscopy, including pharmaceuticals and materials science. These fields require precise molecular characterization while streamlining the spectrum calculation process and offering capabilities to handle a variety of systems.

As we move forward, we anticipate further enhancements to THeSeuSS, integrating additional computational methods and expanding its capabilities through machine learning techniques. These improvements aim to expedite the simulation of vibrational spectra and enable the handling of larger, more complex systems, such as biological molecules and polymers. Ongoing development, driven by user feedback and technological advancements, will ensure that THeSeuSS remains at the forefront of computational spectroscopy tools.

6 | Computational Details

PBE, PBE + MBD-NL, PBE0, PBE0 + MBD-NL and B3LYP calculations were performed using the all-electron numeric-atom-centered orbital code FHI-aims (Fritz Haber Institute ab initio molecular simulations) [33, 34, 36, 87, 88, 129–131]. Scalar relativistic effects were included using the zero-order regular approximation (ZORA), in the case of PBE and PBE + MBD-NL. The tight species default settings in FHI-aims were applied for all numerical atom-centered basis functions and integration grids. Convergence criteria of 10^{-6} eV for total energy, 10^{-7} electrons/Å^3 for charge density, 10^{-5} eV/Å for the sum of eigenvalues, and 10^{-4} eV for forces were employed. In cases of cell and geometry optimization, the maximum residual force component per atom, below which the geometry relaxation is considered converged was set to 10^{-5} eV/Å, while the maximum acceptable energy increase per relaxation step was also set to 10^{-5} eV. These values were determined after performing convergence tests for total energy, pressure, stresses, and atomic forces. For ammonia and ibuprofen, the Brillouin zone was sampled with a 4×4×4 and 2×3×3 Monkhorst-Pack *k*-points grid, respectively [132].

DFTB3 + MBD calculations were performed using the DFTB+ simulation package [51, 94]. The 3ob-3-1 parameter set, part of the third-order parametrization for organic and biological systems (3OB), was employed [133–136]. The self-consistent cycle stopping criterion was set at 10^{-7} eV. During cell and geometry optimization, the process is halted when the maximal absolute value of the force component drops below 10^{-5} eV/Å. For ammonia and ibuprofen, the Brillouin zone was sampled using a

5 × 5 × 5 and 2 × 3 × 3 Monkhorst-Pack *k*-points grid, respectively [132]. MBD interactions were evaluated using a simpler 1 × 1 × 1 *k*-point mesh with $\beta = 0.83$.

In both periodic and non-periodic cases, the displacement values used in the finite displacement method adhere to PHONOPY's default settings: 0.01 Å for simulations run with FHI-aims, 0.005 Å for those utilizing DFTB+, and 0.01 Å for simulations run with SO3LR. For the graphical representation of the vibrational spectra, we employed Lorentzian broadening with the full width at half maximum (FWHM) set to 10.0.

Author Contributions

Ariadni Boziki: conceptualization (lead), data curation (lead), formal analysis (lead), investigation (lead), methodology (lead), resources (lead), software (lead), validation (lead), writing – original draft (lead), writing – review and editing (equal). **Frédéric Ngono Mebenga:** conceptualization (supporting), methodology (supporting), writing – review and editing (supporting). **Philippe Fernandes:** conceptualization (supporting), methodology (supporting), writing – review and editing (supporting). **Alexandre Tkatchenko:** conceptualization (lead), funding acquisition (lead), project administration (lead), supervision (lead), writing – review and editing (supporting).

Acknowledgments

The authors extend their gratitude to Dr. Olympia Giannou for her insightful discussions regarding coding queries. Special thanks are also due to Dr. Matteo Barborini for his valuable insights into the code and to Dr. Georgios Kafanas for his guidance on parallelization techniques using slurm. The authors are also grateful to Kyunghoon Han for his assistance with mathematical formulations. Lastly, heartfelt thanks are extended to Dr. Benjamin Hourahine and Dr. Mariana Rossi for their invaluable discussions on the intricacies of the DFTB+ and FHI-aims codes, respectively. The calculations presented in this paper were carried out using the HPC facilities of the University of Luxembourg (see hpc.uni.lu) [137], and the Luxembourg national supercomputer MeluXina. A.B. and A.T. gratefully acknowledge the HPC and LuxProvide teams for their expert support.

Conflicts of Interest

The authors declare no conflicts of interest.

Data Availability Statement

THeSeuSS is available as an open-source package through its GitHub repository: {https://github.com/Ariadni20/THeSeuSS}. Comprehensive documentation can be accessed at: {https://ariadni20.github.io/THeSeuSS/}. Additional benchmark data, including computed frequencies, frequency shifts (expressed as percentages), and the MAPE for the H_2O and glycine molecules in the gas phase, are provided in the Data S1.

Related WIREs Articles

Vibrational spectroscopy by means of first-principles molecular dynamics simulations

References

1. P. Larkin, *Infrared and Raman Spectroscopy: Principles and Spectral Interpretation* (Elsevier, 2017).

2. B. Schrader, *Infrared and Raman Spectroscopy: Methods and Applications* (Verlag Chemie, 1995).

3. L. Ho, M. Pepper, and P. Taday, "Signatures and Fingerprints," *Nature Photonics* 2, no. 9 (2008): 541–543.

4. J. Neugebauer, M. Reiher, C. Kind, and B. A. Hess, "Quantum Chemical Calculation of Vibrational Spectra of Large Molecules-Raman and IR Spectra for Buckminsterfullerene," *Journal of Computational Chemistry* 23, no. 9 (2002): 895–910.

5. A. Esser, S. Belsare, D. Marx, and T. Head-Gordon, "Mode Specific THz Spectra of Solvated Amino Acids Using the AMOEBA Polarizable Force Field," *Physical Chemistry Chemical Physics* 19 (2017): 5579–5590.

6. F. Gabas, R. Conte, and M. Ceotto, "Semiclassical Vibrational Spectroscopy of Biological Molecules Using Force Fields," *Journal of Chemical Theory and Computation* 16, no. 6 (2020): 3476–3485.

7. A. M. Reilly and A. Tkatchenko, "Role of Dispersion Interactions in the Polymorphism and Entropic Stabilization of the Aspirin Crystal," *Physical Review Letters* 113 (2014): 055701.

8. E. Ditler and S. Luber, "Vibrational Spectroscopy by Means of First-Principles Molecular Dynamics Simulations," *Wiley Interdisciplinary Reviews: Computational Molecular Science* 12, no. 5 (2022): e1605.

9. F. Billes, I. Ziegler, and H. Mikosch, "Application of Quantum Chemistry for the Interpretation of Vibrational Spectra," *Structural Chemistry* 26 (2015): 1703–1714.

10. J. M. L. Martin and P. R. Taylor, "Structure and Vibrations of Small Carbon Clusters From Coupled-Cluster Calculations," *Journal of Physical Chemistry* 100, no. 15 (1996): 6047–6056.

11. J. V. da Silva Jr, L. N. Vidal, P. A. M. Vazquez, and R. E. Bruns, "Coupled Cluster and Configuration Interaction Quantum Calculations of Infrared Fundamental Intensities," *International Journal of Quantum Chemistry* 110, no. 11 (2010): 2029–2036.

12. M. A. Palafox, "DFT Computations on Vibrational Spectra: Scaling Procedures to Improve the Wavenumbers," *Physical Sciences Reviews* 3, no. 6 (2018): 20170184.

13. M. D. King, W. D. Buchanan, and T. M. Korter, "Identification and Quantification of Polymorphism in the Pharmaceutical Compound Diclofenac Acid by Terahertz Spectroscopy and Solid-State Density Functional Theory," *Analytical Chemistry* 83, no. 10 (2011): 3786–3792.

14. M. T. Ruggiero, J. Sibik, J. A. Zeitler, and T. M. Korter, "Examination of l-Glutamic Acid Polymorphs by Solid-State Density Functional Theory and Terahertz Spectroscopy," *Journal of Physical Chemistry A* 120, no. 38 (2016): 7490–7495.

15. M. P. Davis and T. M. Korter, "Low-Frequency Vibrational Spectroscopy and Quantum Mechanical Simulations of the Crystalline Polymorphs of the Antiviral Drug Ribavirin," *Molecular Pharmaceutics* 19, no. 9 (2022): 3385–3393.

16. K. C. Oppenheim, T. M. Korter, J. S. Melinger, and D. Grischkowsky, "Solid-State Density Functional Theory Investigation of the Terahertz Spectra of the Structural Isomers 1,2-Dicyanobenzene and 1,3-Dicyanobenzene," *Journal of Physical Chemistry A* 114, no. 47 (2010): 12513–12521.

17. I. M. Alecu, J. Zheng, Y. Zhao, and D. G. Truhlar, "Computational Thermochemistry: Scale Factor Databases and Scale Factors for Vibrational Frequencies Obtained From Electronic Model Chemistries," *Journal of Chemical Theory and Computation* 6, no. 9 (2010): 2872–2887.

18. T. M. Kolev, E. A. Velcheva, B. A. Stamboliyska, and M. Spiteller, "DFT and Experimental Studies of the Structure and Vibrational Spectra of Curcumin," *International Journal of Quantum Chemistry* 102, no. 6 (2005): 1069–1079.

19. H. A. Witek, K. Morokuma, and A. Stradomska, "Modeling Vibrational Spectra Using the Self-Consistent Charge Density-Functional Tight-Binding Method. I. Raman Spectra," *Journal of Chemical Physics* 121, no. 11 (2004): 5171–5178.

20. C. Feng, R. Q. Zhang, S. L. Dong, T. A. Niehaus, and T. Frauenheim, "Signatures in Vibrational Spectra of Ice Nanotubes Revealed by a Density Functional Tight Binding Method," *Journal of Physical Chemistry C* 111, no. 38 (2007): 14131–14138.

21. H. A. Witek, K. Morokuma, and A. Stradomska, "Modeling Vibrational Spectra Using the Self-Consistent Charge Density-Functional Tight-Binding Method II: Infrared Spectra," *Journal of Theoretical and Computational Chemistry* 04, no. spec01 (2005): 639–655.

22. H. Yu and Q. Cui, "The Vibrational Spectra of Protonated Water Clusters: A Benchmark for Self-Consistent-Charge Density-Functional Tight Binding," *Journal of Chemical Physics* 127, no. 23 (2007): 234504.

23. E. Małolepsza, H. A. Witek, and K. Morokuma, "Accurate Vibrational Frequencies Using the Self-Consistent-Charge Density-Functional Tight-Binding Method," *Chemical Physics Letters* 412, no. 4 (2005): 237–243.

24. R. Han, R. Ketkaew, and S. Luber, "A Concise Review on Recent Developments of Machine Learning for the Prediction of Vibrational Spectra," *Journal of Physical Chemistry A* 126, no. 6 (2022): 801–812.

25. S. Ye, K. Zhong, J. Zhang, et al., "A Machine Learning Protocol for Predicting Protein Infrared Spectra," *Journal of the American Chemical Society* 142, no. 45 (2020): 19071–19077.

26. B. Nebgen, N. Lubbers, J. S. Smith, et al., "Transferable Dynamic Molecular Charge Assignment Using Deep Neural Networks," *Journal of Chemical Theory and Computation* 14, no. 9 (2018): 4687–4698.

27. M. Gastegger, J. Behler, and P. Marquetand, "Machine Learning Molecular Dynamics for the Simulation of Infrared Spectra," *Chemical Science* 8 (2017): 6924–6935.

28. N. Raimbault, A. Grisafi, M. Ceriotti, and M. Rossi, "Using Gaussian Process Regression to Simulate the Vibrational Raman Spectra of Molecular Crystals," *New Journal of Physics* 21, no. 10 (2019): 105001.

29. S. Lifson and A. Warshel, "Consistent Force Field for Calculations of Conformations, Vibrational Spectra, and Enthalpies of Cycloalkane and n-Alkane Molecules," *Journal of Chemical Physics* 49, no. 11 (1968): 5116–5129.

30. E. Małolepsza and J. E. Straub, "Empirical Maps for the Calculation of Amide I Vibrational Spectra of Proteins From Classical Molecular Dynamics Simulations," *Journal of Physical Chemistry B* 118, no. 28 (2014): 7848–7855.

31. A. Togo, "First-Principles Phonon Calculations With Phonopy and phono3py," *Journal of the Physical Society of Japan* 92, no. 1 (2023): 012001.

32. A. Togo, L. Chaput, T. Tadano, and I. Tanaka, "Implementation Strategies in Phonopy and phono3py," *Journal of Physics: Condensed Matter* 35, no. 35 (2023): 353001.

33. V. Blum, R. Gehrke, F. Hanke, et al., "Ab Initio Molecular Simulations With Numeric Atom-Centered Orbitals," *Computer Physics Communications* 180, no. 11 (2009): 2175–2196.

34. V. Havu, V. Blum, P. Havu, and M. Scheffler, "Efficient O(N) Integration for All-Electron Electronic Structure Calculation Using Numeric Basis Functions," *Journal of Computational Physics* 228, no. 22 (2009): 8367–8379.

35. A. Marek, V. Blum, R. Johanni, et al., "The ELPA Library: Scalable Parallel Eigenvalue Solutions for Electronic Structure Theory and Computational Science," *Journal of Physics: Condensed Matter* 26, no. 21 (2014): 213201.

36. V. W. Yu, F. Corsetti, A. García, et al., "ELSI: A Unified Software Interface for Kohn–Sham Electronic Structure Solvers," *Computer Physics Communications* 222 (2018): 267–285.

37. V. W. Yu, C. Campos, W. Dawson, et al., "ELSI—An Open Infrastructure for Electronic Structure Solvers," *Computer Physics Communications* 256 (2020): 107459.

38. P. Giannozzi, S. Baroni, N. Bonini, et al., "QUANTUM ESPRESSO: A Modular and Open-Source Software Project for Quantum Simulations of Materials," *Journal of Physics: Condensed Matter* 21, no. 39 (2009): 395502.

39. P. Giannozzi, O. Andreussi, T. Brumme, et al., "Advanced Capabilities for Materials Modelling With Quantum ESPRESSO," *Journal of Physics: Condensed Matter* 29, no. 46 (2017): 465901.

40. M. J. Frisch, G. W. Trucks, H. B. Schlegel, et al., *Gaussian 16 Revision C.01* (Gaussian Inc, 2016).

41. G. M. J. Barca, C. Bertoni, L. Carrington, et al., "Recent Developments in the General Atomic and Molecular Electronic Structure System," *Journal of Chemical Physics* 152, no. 15 (2020): 154102.

42. F. Neese, F. Wennmohs, U. Becker, and C. Riplinger, "The ORCA Quantum Chemistry Program Package," *Journal of Chemical Physics* 152, no. 22 (2020): 224108.

43. F. Furche, R. Ahlrichs, C. Hättig, W. Klopper, M. Sierka, and F. Weigend, "Turbomole," *Wiley Interdisciplinary Reviews: Computational Molecular Science* 4, no. 2 (2014): 91–100.

44. T. D. Kühne, M. Iannuzzi, M. Del Ben, et al., "CP2K: An Electronic Structure and Molecular Dynamics Software Package - Quickstep: Efficient and Accurate Electronic Structure Calculations," *Journal of Chemical Physics* 152, no. 19 (2020): 194103.

45. E. Artacho, D. Sánchez-Portal, P. Ordejón, A. García, and J. M. Soler, "Linear-Scaling Ab-Initio Calculations for Large and Complex Systems," *Physica Status Solidi B* 215, no. 1 (1999): 809–817.

46. E. Artacho, E. Anglada, O. Diéguez, et al., "The SIESTA Method; Developments and Applicability," *Journal of Physics: Condensed Matter* 20, no. 6 (2008): 064208.

47. J. M. Soler, E. Artacho, J. D. Gale, et al., "The SIESTA Method for Ab Initio Order-N Materials Simulation," *Journal of Physics: Condensed Matter* 14, no. 11 (2002): 2745–2779.

48. X. Gonze, F. Jollet, F. A. Araujo, et al., "Recent Developments in the ABINIT Software Package," *Computer Physics Communications* 205 (2016): 106–131.

49. X. Gonze, J. M. Beuken, R. Caracas, et al., "First-Principles Computation of Material Properties: The ABINIT Software Project," *Computational Materials Science* 25, no. 3 (2002): 478–492.

50. S. J. Clark, M. D. Segall, C. J. Pickard, et al., "First Principles Methods Using CASTEP," *Zeitschrift fur Kristallographie - Crystalline Materials* 220, no. 5–6 (2005): 567–570.

51. B. Hourahine, B. Aradi, V. Blum, et al., "DFTB+, A Software Package for Efficient Approximate Density Functional Theory Based Atomistic Simulations," *Journal of Chemical Physics* 152, no. 12 (2020): 124101.

52. A. P. Thompson, H. M. Aktulga, R. Berger, et al., "LAMMPS - a Flexible Simulation Tool for Particle-Based Materials Modeling at the Atomic, Meso, and Continuum Scales," *Computer Physics Communications* 271 (2022): 108171.

53. M. Thomas, M. Brehm, R. Fligg, P. Vöhringer, and B. Kirchner, "Computing Vibrational Spectra From Ab Initio Molecular Dynamics," *Physical Chemistry Chemical Physics* 15 (2013): 6608–6622.

54. M. Thomas, M. Brehm, and B. Kirchner, "Voronoi Dipole Moments for the Simulation of Bulk Phase Vibrational Spectra," *Physical Chemistry Chemical Physics* 17 (2015): 3207–3213.

55. N. T. Hung, J. Huang, Y. Tatsumi, T. Yang, and R. Saito, "QERaman: An Open-Source Program for Calculating Resonance Raman Spectra Based on Quantum ESPRESSO," *Computer Physics Communications* 295 (2024): 108967.

56. S. S. Khire, N. Sahu, and S. R. Gadre, "MTASpec Software for Calculating the Vibrational IR and Raman Spectra of Large Molecules

at Ab Initio Level," *Computer Physics Communications* 270 (2022): 108175.

57. L. Bastonero and N. Marzari, "Automated All-Functionals Infrared and Raman Spectra," *npj Computational Materials* 10, no. 1 (2024): 55.

58. A. Kabylda, J. T. Frank, S. S. Dou, et al., *Molecular Simulations With a Pretrained Neural Network and Universal Pairwise Force Fields* (ChemRxiv, 2024).

59. T. Frank, O. Unke, K. R. Müller, and S. Chmiela, "A Euclidean Transformer for Fast and Stable Machine Learned Force Fields," *Nature Communications* 15, no. 1 (2024): 6539.

60. B. H. Stuart, *Infrared Spectroscopy: Fundamentals and Applications* (John Wiley & Sons, 2004).

61. B. Stuart, *Infrared Spectroscopy* (John Wiley & Sons, Ltd, 2005).

62. E. Smith and G. Dent, *Modern Raman Spectroscopy: A Practical Approach* (John Wiley & Sons, 2019).

63. G. Keresztury, "Raman Spectroscopy: Theory," in *Handbook of Vibrational Spectroscopy* (Wiley, 2006).

64. V. Heine and D. Weaire, *Solid State Physics*, vol. 24, ed. H. Ehrenreich, F. Seitz, and D. Turnbull (Academic Press, 1970), 249.

65. S. Baroni, P. Giannozzi, and A. Testa, "Green's-Function Approach to Linear Response in Solids," *Physical Review Letters* 58 (1987): 1861–1864.

66. X. Gonze and J. P. Vigneron, "Density-Functional Approach to Nonlinear-Response Coefficients of Solids," *Physical Review B* 39 (1989): 13120–13128.

67. P. Giannozzi, S. de Gironcoli, P. Pavone, and S. Baroni, "Ab Initio Calculation of Phonon Dispersions in Semiconductors," *Physical Review B: Condensed Matter* 43 (1991): 7231–7242.

68. S. Y. Savrasov, "Linear-Response Theory and Lattice Dynamics: A Muffin-Tin-Orbital Approach," *Physical Review B* 54 (1996): 16470–16486.

69. X. Gonze and C. Lee, "Dynamical Matrices, Born Effective Charges, Dielectric Permittivity Tensors, and Interatomic Force Constants From Density-Functional Perturbation Theory," *Physical Review B* 55 (1997): 10355–10368.

70. S. Baroni, S. de Gironcoli, A. Dal Corso, and P. Giannozzi, "Phonons and Related Crystal Properties From Density-Functional Perturbation Theory," *Reviews of Modern Physics* 73 (2001): 515–562.

71. A. Ratnaparkhe and W. R. L. Lambrecht, "Calculated Phonon Modes, Infrared, and Raman Spectra in $ZnGeGa_2N_4$," *Journal of Applied Physics* 128, no. 7 (2020): 075702.

72. A. Ratnaparkhe, S. Kumar Radha, and W. R. L. Lambrecht, "Calculated Phonon Modes, Infrared and Raman Spectra in Orthorhombic α-MoO_3 and Monolayer MoO_3," *Journal of Applied Physics* 130, no. 10 (2021): 104302.

73. P. J. Larkin, "Chapter 6—IR and Raman Spectra–Structure Correlations: Characteristic Group Frequencies," in *Infrared and Raman Spectroscopy*, 2nd ed., ed. P. J. Larkin (Elsevier, 2018), 85–134.

74. D. Porezag and M. R. Pederson, "Infrared Intensities and Raman-Scattering Activities Within Density-Functional Theory," *Physical Review B* 54 (1996): 7830–7836.

75. R. D. King-Smith and D. Vanderbilt, "Theory of Polarization of Crystalline Solids," *Physical Review B* 47 (1993): 1651–1654.

76. R. Resta, "Macroscopic Polarization in Crystalline Dielectrics: The Geometric Phase Approach," *Reviews of Modern Physics* 66 (1994): 899–915.

77. N. Marzari and D. Vanderbilt, "Maximally Localized Generalized Wannier Functions for Composite Energy Bands," *Physical Review B* 56 (1997): 12847–12865.

78. P. L. Silvestrelli and M. Parrinello, "Structural, Electronic, and Bonding Properties of Liquid Water From First Principles," *Journal of Chemical Physics* 111, no. 8 (1999): 3572–3580.

79. P. L. Silvestrelli and M. Parrinello, "Water Molecule Dipole in the Gas and in the Liquid Phase," *Physical Review Letters* 82 (1999): 3308–3311.

80. N. Raimbault, V. Athavale, and M. Rossi, "Anharmonic Effects in the Low-Frequency Vibrational Modes of Aspirin and Paracetamol Crystals," *Physical Review Materials* 3 (2019): 053605.

81. X. Gonze, "First-Principles Responses of Solids to Atomic Displacements and Homogeneous Electric Fields: Implementation of a Conjugate-Gradient Algorithm," *Physical Review B* 55 (1997): 10337–10354.

82. D. Maag, J. Böser, H. A. Witek, B. Hourahine, M. Elstner, and T. Kubař, "Mechanism of Proton-Coupled Electron Transfer Described With QM/MM Implementation of Coupled-Perturbed Density-Functional Tight-Binding," *Journal of Chemical Physics* 158, no. 12 (2023): 124107.

83. A. Togo and I. Tanaka, "Spglib: A Software Library for Crystal Symmetry Search," 2018 arXiv preprint arXiv: 180801590.

84. THeSeuSS documentation, "Welcome to THeSeuSS," https://ariadni20.github.io/THeSeuSS/.

85. A. la Otero-de- Roza and E. R. Johnson, "A Benchmark for Non-Covalent Interactions in Solids," *Journal of Chemical Physics* 137, no. 5 (2012): 054103.

86. A. M. Reilly and A. Tkatchenko, "Understanding the Role of Vibrations, Exact Exchange, and Many-Body van der Waals Interactions in the Cohesive Properties of Molecular Crystals," *Journal of Chemical Physics* 139, no. 2 (2013): 024705.

87. J. P. Perdew, K. Burke, and M. Ernzerhof, "Generalized gradient approximation made simple," *Physical Review Letters* 77 (1996): 3865–3868.

88. J. Hermann and A. Tkatchenko, "Density Functional Model for van der Waals Interactions: Unifying Many-Body Atomic Approaches With Nonlocal Functionals," *Physical Review Letters* 124 (2020): 146401.

89. A. M. Reilly, R. I. Cooper, C. S. Adjiman, et al., "Report on the Sixth Blind Test of Organic Crystal Structure Prediction Methods," *Acta Crystallographica. Section B: Structural Science, Crystal Engineering and Materials* 72, no. 4 (2016): 439–459.

90. G. M. Day, T. G. Cooper, A. J. Cruz-Cabeza, et al., "Significant Progress in Predicting the Crystal Structures of Small Organic Molecules-a Report on the Fourth Blind Test," *Acta Crystallographica. Section B: Structural Science, Crystal Engineering and Materials* 65, no. 2 (2009): 107–125.

91. D. A. Bardwell, C. S. Adjiman, Y. A. Arnautova, et al., "Towards Crystal Structure Prediction of Complex Organic Compounds-a Report on the Fifth Blind Test," *Acta Crystallographica. Section B: Structural Science, Crystal Engineering and Materials* 67, no. 6 (2011): 535–551.

92. J. Hoja, H. Y. Ko, M. A. Neumann, R. Car, R. A. DiStasio, and A. Tkatchenko, "Reliable and Practical Computational Description of Molecular Crystal Polymorphs," *Science Advances* 5, no. 1 (2019): eaau3338.

93. C. Adamo and V. Barone, "Toward Reliable Density Functional Methods Without Adjustable Parameters: The PBE0 Model," *Journal of Chemical Physics* 110, no. 13 (1999): 6158–6170.

94. A. Tkatchenko, R. A. DiStasio, R. Car, and M. Scheffler, "Accurate and Efficient Method for Many-Body van der Waals Interactions," *Physical Review Letters* 108, no. 23 (2012): 236402.

95. R. A. DiStasio Jr, O. A. von Lilienfeld, and A. Tkatchenko, "Collective Many-Body van der Waals Interactions in Molecular Systems," *Proceedings of the National Academy of Sciences of the United States of America* 109, no. 37 (2012): 14791–14795.

96. A. Ambrosetti, A. M. Reilly, R. A. DiStasio, and A. Tkatchenko, "Long-Range Correlation Energy Calculated From Coupled Atomic Response Functions," *Journal of Chemical Physics* 140, no. 18 (2014): 18A508.

97. R. A. DiStasio, V. V. Gobre, and A. Tkatchenko, "Many-Body van der Waals Interactions in Molecules and Condensed Matter," *Journal of Physics. Condensed Matter* 26, no. 21 (2014): 213202.

98. C. Lee, W. Yang, and R. G. Parr, "Development of the Colle-Salvetti Correlation-Energy Formula Into a Functional of the Electron Density," *Physical Review B* 37 (1988): 785–789.

99. A. D. Becke, "Density-Functional Thermochemistry. III. The Role of Exact Exchange," *Journal of Chemical Physics* 98, no. 7 (1993): 5648–5652.

100. J. C. Howard, J. L. Gray, A. J. Hardwick, L. T. Nguyen, and G. S. Tschumper, "Getting Down to the Fundamentals of Hydrogen Bonding: Anharmonic Vibrational Frequencies of $(HF)_2$ and $(H_2O)_2$ from Ab Initio Electronic Structure Computations," *Journal of Chemical Theory and Computation* 10, no. 12 (2014): 5426–5435.

101. J. C. Howard and G. S. Tschumper, "Benchmark Structures and Harmonic Vibrational Frequencies Near the CCSD(T) Complete Basis Set Limit for Small Water Clusters: $(H_2O)_{n=2,3,4,5,6}$," *Journal of Chemical Theory and Computation* 11, no. 5 (2015): 2126–2136.

102. J. C. Howard and G. S. Tschumper, "N-Body:Many-Body QM:QM Vibrational Frequencies: Application to Small Hydrogen-Bonded Clusters," *Journal of Chemical Physics* 139, no. 18 (2013): 184113.

103. E. Miliordos, E. Aprà, and S. S. Xantheas, "Optimal Geometries and Harmonic Vibrational Frequencies of the Global Minima of Water Clusters $(H_2O)_n$, $n = 2$-6, and Several Hexamer Local Minima at the CCSD(T) Level of Theory," *Journal of Chemical Physics* 139, no. 11 (2013): 114302.

104. Y. Wang, X. Huang, B. C. Shepler, B. J. Braams, and J. M. Bowman, "Flexible, Ab Initio Potential, and Dipole Moment Surfaces for Water. I. Tests and Applications for Clusters up to the 22-Mer," *Journal of Chemical Physics* 134, no. 9 (2011): 094509.

105. Y. Wang, B. C. Shepler, B. J. Braams, and J. M. Bowman, "Full-Dimensional, Ab Initio Potential Energy and Dipole Moment Surfaces for Water," *Journal of Chemical Physics* 131, no. 5 (2009): 054511.

106. A. A. Kananenka and J. L. Skinner, "Fermi Resonance in OH-Stretch Vibrational Spectroscopy of Liquid Water and the Water Hexamer," *Journal of Chemical Physics* 148, no. 24 (2018): 244107.

107. N. F. Zobov, O. L. Polyansky, C. R. Le Sueur, and J. Tennyson, "Vibration-Rotation Levels of Water Beyond the Born-Oppenheimer Approximation," *Chemical Physics Letters* 260, no. 3 (1996): 381–387.

108. M. Falk, "The Frequency of the H-O-H Bending Fundamental in Solids and Liquids," *Spectrochimica Acta A* 40, no. 1 (1984): 43–48.

109. M. Gaus, Q. Cui, and M. Elstner, "Density Functional Tight Binding: Application to Organic and Biological Molecules," *Wiley Interdisciplinary Reviews: Computational Molecular Science* 4, no. 1 (2014): 49–61.

110. T. J. Giese and D. M. York, "Charge-Dependent Model for Many-Body Polarization, Exchange, and Dispersion Interactions in Hybrid Quantum Mechanical Molecular Mechanical Calculations," *Journal of Chemical Physics* 127, no. 19 (2007): 194101.

111. P. Goyal, H. J. Qian, S. Irle, et al., "Molecular Simulation of Water and Hydration Effects in Different Environments: Challenges and Developments for DFTB Based Models," *Journal of Physical Chemistry B* 118, no. 38 (2014): 11007–11027.

112. M. P. Lourenço, E. C. dos Santos, L. G. M. Pettersson, and H. A. Duarte, "Accurate SCC-DFTB Parametrization for Bulk Water," *Journal of Chemical Theory and Computation* 16, no. 3 (2020): 1768–1778.

113. S. Jahangiri, L. Cai, and G. H. Peslherbe, "Performance of Density-Functional Tight-Binding Models in Describing Hydrogen-Bonded Anionic-Water Clusters," *Journal of Computational Chemistry* 35, no. 23 (2014): 1707–1715.

114. V. Q. Vuong and Q. Cui, "Reparameterization of the Chemical-Potential Equalization Model With DFTB3: A Practical Balance Between Accuracy and Transferability," *Journal of Chemical Physics* 158, no. 6 (2023): 064111.

115. N. Cinq, A. Simon, F. Louisnard, and J. Cuny, "Accurate SCC-DFTB Parametrization of Liquid Water With Improved Atomic Charges and Iterative Boltzmann Inversion," *Journal of Physical Chemistry B* 127, no. 35 (2023): 7590–7601.

116. S. G. Stepanian, I. D. Reva, E. D. Radchenko, et al., "Matrix-Isolation Infrared and Theoretical Studies of the Glycine Conformers," *Journal of Physical Chemistry. A* 102, no. 6 (1998): 1041–1054.

117. S. Kumar, A. K. Rai, V. B. Singh, and S. B. Rai, "Vibrational Spectrum of Glycine Molecule," *Spectrochimica Acta Part A, Molecular and Biomolecular Spectroscopy* 61, no. 11 (2005): 2741–2746.

118. Y. Grenie and C. Garrigou-Lagrange, "Infrared Spectra of Glycine Isotopic Species Isolated in an Argon or Nitrogen Matrix," *Journal of Molecular Spectroscopy* 41, no. 2 (1972): 240–248.

119. S. Suzuki, T. Shimanouchi, and M. Tsuboi, "Normal Vibrations of Glycine and Deuterated Glycine Molecules," *Spectrochimica Acta* 19, no. 7 (1963): 1195–1208.

120. J. S. Holt, D. Sadoskas, and C. J. Pursell, "Infrared Spectroscopy of the Solid Phases of Ammonia," *Journal of Chemical Physics* 120, no. 15 (2004): 7153–7157.

121. C. L. Nye and F. D. Medina, "Temperature Dependence of the Raman Spectrum of Ammonia Solid I," *Journal of Chemical Physics* 87, no. 12 (1987): 6890–6894.

122. W. Zheng and R. I. Kaiser, "An Infrared Spectroscopy Study of the Phase Transition in Solid Ammonia," *Chemical Physics Letters* 440, no. 4 (2007): 229–234.

123. J. R. Ferraro, G. Sill, and U. Fink, "Infrared Intensity Measurements of Cryodeposited Thin Films of NH_3, NH_4HS, H_2S, and Assignments of Absorption Bands," *Applied Spectroscopy* 34, no. 5 (1980): 525–533.

124. M. Gauthier, P. Pruzan, J. M. Besson, G. Hamel, and G. Syfosse, "Investigation of the Phase Diagram of Ammonia by Raman Scattering," *Physica B+C* 139–140 (1986): 218–220.

125. O. S. Binbrek and A. Anderson, "Raman Spectra of Molecular Crystals. Ammonia and 3-Deutero-Ammonia," *Chemical Physics Letters* 15, no. 3 (1972): 421–427.

126. L. Huang, Y. Han, J. Liu, X. He, and J. Li, "Ab Initio Prediction of the Phase Transition for Solid Ammonia at High Pressures," *Scientific Reports* 10 (2020): 7546.

127. T. Kume, S. Sasaki, and H. Shimizu, "Raman Study of Solid Ammonia at High Pressures and Low Temperatures," *Journal of Raman Specroscopy* 32, no. 5 (2001): 383–387.

128. S. Ramukutty and E. Ramachandran, "Growth, Spectral and Thermal Studies of Ibuprofen Crystals," *Crystal Research and Technology* 47, no. 1 (2012): 31–38.

129. F. Knuth, C. Carbogno, V. Atalla, V. Blum, and M. Scheffler, "All-Electron Formalism for Total Energy Strain Derivatives and Stress Tensor Components for Numeric Atom-Centered Orbitals," *Computer Physics Communications* 190 (2015): 33–50.

130. X. Ren, P. Rinke, V. Blum, et al., "Resolution-Of-Identity Approach to Hartree–Fock, Hybrid Density Functionals, RPA, MP2 and GW With Numeric Atom-Centered Orbital Basis Functions," *New Journal of Physics* 14, no. 5 (2012): 053020.

131. A. C. Ihrig, J. Wieferink, I. Y. Zhang, et al., "Accurate Localized Resolution of Identity Approach for Linear-Scaling Hybrid Density Functionals and for Many-Body Perturbation Theory," *New Journal of Physics* 17, no. 9 (2015): 093020.

132. H. J. Monkhorst and J. D. Pack, "Special Points for Brillouin-Zone Integrations," *Physical Review B* 13, no. 12 (1976): 5188–5192.

133. M. Gaus, A. Goez, and M. Elstner, "Parametrization and Benchmark of DFTB3 for Organic Molecules," *Journal of Chemical Theory and Computation* 9 (2013): 338–354.

134. M. Gaus, X. Lu, M. Elstner, and Q. Cui, "Parameterization of DFTB3/3OB for Sulfur and Phosphorus for Chemical and Biological Applications," *Journal of Chemical Theory and Computation* 10 (2014): 1518–1537.

135. X. Lu, M. Gaus, M. Elstner, and Q. Cui, "Parametrization of DFTB3/3OB for Magnesium and Zinc for Chemical and Biological Applications," *Journal of Physical Chemistry B* 119 (2015): 1062–1082.

136. M. Kubillus, T. Kubař, M. Gaus, J. Řezáč, and M. Elstner, "Parameterization of the DFTB3 Method for Br, Ca, Cl, F, I, K, and Na in Organic and Biological Systems," *Journal of Chemical Theory and Computation* 11 (2015): 332–342.

137. S. Varrette, P. Bouvry, H. Cartiaux, and F. Georgatos, "Management of an Academic HPC Cluster: The UL Experience," in *2014 International Conference on High Performance Computing & Simulation (HPCS)* (IEEE, 2014), 959–967.

Supporting Information

Additional supporting information can be found online in the Supporting Information section.